Relative electron inelastic mean free paths for diamond and graphite at 8 keV and intrinsic contributions to the energy-loss

C. Kunz[a,*], B.C.C. Cowie[b], W. Drube[c], T.-L. Lee[d], S. Thiess[c], C. Wild[e], J. Zegenhagen[f]

[a] *Inst. f. Exp. Physik University Hamburg, Luruper Ch. 149, D-22761 Hamburg, Germany*
[b] *Australian Synchrotron, 800 Blackburn Rd, Clayton, VIC 3168, Australia*
[c] *Deutsches Elektronen Synchrotron, DESY, D-22607 Hamburg, Germany*
[d] *Diamond Light Source Ltd., Didcot, Oxfordshire OX11 0DE, United Kingdom*
[e] *Fraunhofer-Inst. f. Angew. Festkörperphysik, IAF, Tullastraße 72, D-79108 Freiburg, Germany*
[f] *ESRF, F-38043 Grenoble Cedex, France*

Article history:
Received 14 January 2009
Received in revised form 19 March 2009
Accepted 28 March 2009
Available online 7 April 2009

Keywords:
Hard X-ray photoemission
Synchrotron radiation
Electron attenuation lengths
Diamond
Graphite

A B S T R A C T

We used hard X-ray photoelectron spectroscopy (HAXPES) with 8 keV X-rays to investigate the 1s emission of carbon. We recorded spectra extending from the peak of the C 1s electrons ("elastic" line) to electrons with up to 110 eV energy-loss. Using two samples side by side, we could compare the inelastic mean free paths (IMFPs) of the electrons of almost 8 keV in diamond and graphite and find them to be practically identical despite about 50% difference in densities. Published extrapolations of their IMFP calculations at lower energies are in good agreement with this result. We show that information from the almost structureless region of overlapping multiple extrinsic energy-losses can be used to quantify the fraction of photoelectrons experiencing intrinsic energy-losses (those due to the sudden creation of the hole). We find that this fraction is 58% of the primary excited C 1s electrons for diamond and is practically the same for graphite. This is at first sight an unexpected result since hole-screening should differ in a semimetal from that in an insulator. The observation can be accounted for by dynamic screening in contrast to static screening.

1. Introduction

Hard X-ray photoelectron spectroscopy (HAXPES) is a new and rapidly evolving field of research. The increased inelastic mean free path (IMFP) of the emitted electrons with high kinetic energy facilitates investigations of chemical properties and electronic states in the bulk of materials and at buried interfaces. Because of the small cross-sections it can only be fully exploited with the highly monochromatic X-ray flux at 3rd generation synchrotron radiation facilities. The research done so far was summarized at two international workshops, HAXPES 1 which took place in Grenoble, 2003, France and HAXPES 2 which took place at Spring-8, 2006, Harima Garden City, Japan. Proceedings of the first workshop [1] are available and give a good overview of the field. A major issue is the utilization of the large inelastic mean free path (IMFP) of the photoelectrons, i.e., the distance until the electron undergoes an inelastic scattering event and loses energy. For the classical region of photoelectron spectroscopy up to 2 keV a host of measured and calculated data exists due to its intensive application over many years, of which we give here only a few references [2–9]. However, there are relatively few measurements of IMFPs at higher energies, up to 10 keV and above. Thus, research in the area of HAXPES relies at this moment mainly on IMFP values, which are obtained by extrapolating available data (experimental or calculated) for lower energies to higher electron kinetic energies. Bethe [10] has provided the correct energy dependence based on atomic calculations but the appropriate parameters in his equation need to be determined, usually with the help of models making use of optical constants [11,12].

In previous papers [13,14] we have reported measurements of sub-shell cross-sections of gold in the energy range 5–14.5 keV. Particularly interesting are shallow core levels, since the cross-sections in the solid may differ from the values for the free atom. The obtained cross-sections cannot be regarded as being truly absolute, since we obtained them by comparing the photoelectron yield from gold with the yield from a graphite sample as reference measured under the same conditions. Furthermore, such experiments rely on extracting the intensity of the emitted characteristic photoelectrons from the recorded spectra, which we call in the following elastic line. They rely on assuming that the elastic line accounts for a constant fraction of the overall primary excitation rate. However, in addition to the elastic line has to be added the intensity

* Corresponding author.
E-mail address: christof.kunz@gmx.net (C. Kunz).

of those electrons which are emitted at lower energy because of excitation due to incomplete screening of the core hole. These are the so-called intrinsic contributions to the energy-loss. In the spectra the term "primary" throughout this paper comprises the elastic line and the intrinsic losses. The fundamental importance of intrinsic excitations was an additional motivation to determine the intensity of their contribution in the present investigation at 8 keV.

Already in Ref. [14] we have pointed out that comparative measurements with different materials containing the same atomic species could also provide relative IMFPs with good accuracy. This concept was further pursued in the present investigation with carbon in two crystallographic states. The density of diamond is 54% higher than that of graphite thus providing a good means to test equations which use the electron density or the free-electron plasma frequency as the main parameter. The different empirical relationships for extrapolating IMFPs fitted to low energy data are well summarized by Tanuma et al. [4]. We shall make use of a more recent analysis from this group [9] for a comparison with our result. Carbon is a very convenient test case since the total photoelectric cross-section of carbon is dominated by the C 1s orbital and the very small amount of photo-excited valence-band electrons can be safely neglected at 8 keV.

Furthermore, we exploit the energy-loss spectrum beyond the elastic line in the present study. This region is dominated by the overlap of the intrinsic excitations (the satellite structure due to the sudden creation of the hole), first and multiple extrinsic energy-losses (encountered along the electron trajectory) and surface losses. We shall show that, without separating the spectra into their individual components, we can obtain relative IMFPs and determine the fraction of intrinsic excitations during the photoelectron emission process.

The basic idea behind our evaluation is the fact that at high enough energies the majority of electrons which reach the narrow angular acceptance interval of the analyzer will have undergone only small angular deviations from elastic and inelastic scattering events. Even after several scattering events the photoelectrons travel close to a straight line in the direction determined by the analyzer. Nevertheless, the dominant forward-scattering results in a signal which is proportional to the angular integration of the scattering events. This allows performing the analysis analytically, without specific Monte Carlo calculations that are often applied at lower energies where large-angle scattering is of importance (see e.g. [6–8]). The photoelectrons are released by the hard X-ray beam in the carbon samples uniformly over a large depth (>1 μm). Electrons originating at a much smaller depth, which is defined by a small material dependent number of elastic and inelastic scattering events, travel to the surface on almost straight paths. An electron traveling through the material before reaching the surface will undergo extrinsic energy-losses one after another practically with equal probability and thus on average after the same distance. This holds as long as the change in energy is small in comparison with the initial kinetic energy, a condition which is safely fulfilled in the present experiment. With a certain probability primary electrons escape without undergoing an extrinsic energy-loss. Be reminded, primary electrons are those which start at the site of the atom and if having undergone no extrinsic losses show up in the spectra as elastic lines, intrinsic losses and atomic satellites. The equality of the spectral weight of all orders of energy-loss ($n = 0, 1, 2, 3, \ldots$ up to the point where the one-dimensional model breaks down) is the consequence of the constant IMFP leading to a Poisson distribution for the escape probability of electrons originating at a certain depth below the surface. The details of our analysis are explained in chapter 4 and in the appendices.

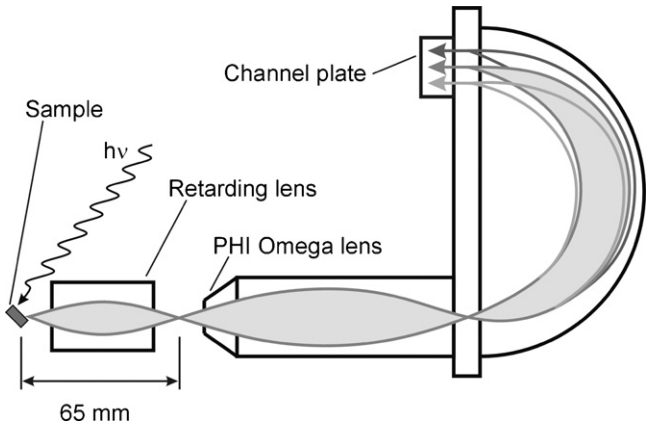

Fig. 1. Scheme of the hemispherical detector PHI 360 with added retarding lens to extend the energy range up to 14.5 keV [13]. Electrons are collected at 45° to the surface.

2. Experimental

As in our previous investigations [13,14] we have performed the present experiments with a commercially available electron spectrometer (PHI 360). This is a hemispherical electron analyzer equipped with a retarding and focusing "Omega" lens and a 16 channel detection system, in front of which we added a home-built supplementary lens. It allowed us to retard the electrons additionally by up to 10 keV. Pre-retarding the electrons required the sample to be kept at high voltages up to 10 kV. To permit sample biasing the sample is insulated. The detector in the PHI 360 analyzer has the advantage that it is equipped with a fast channel-plate detector, counting electrons individually, and thus up to high count-rates (~1 MHz) the count-rate is strictly linear with the electron intensity. This is indispensable for accurate relative intensity measurements. Fig. 1 shows schematically our experimental arrangement. For further details about the employed electron optics see Ref. [13].

A highly oriented pyrolytic graphite (HOPG) sample was freshly cleaved in air, then rapidly transferred into the HAXPES UHV chamber. The diamond sample was produced with the chemical vapor deposition CVD-process [15] at the Fraunhofer Institute for Applied Solid State Physics in Freiburg resulting in a polycrystalline wafer which was subsequently polished with a few nanometer roughness. It was doped with an atomic fraction of 5×10^{-6} boron to render it conductive. No boron signal was detectable in the spectra. The only observed contamination on both samples was a negligibly small signal of oxygen (O 1s).

The atomic densities are taken from crystallographic data to be $\rho_{At}^{D} = 17.6 \times 10^{22}/\mathrm{cm}^3$ for diamond and $\rho_{At}^{C} = 11.4 \times 10^{22}/\mathrm{cm}^3$ for graphite. We are aware that sometimes lower densities are quoted for graphite depending on the origin of the graphite samples. In our case we started with a cleavable HOPG crystal and therefore consider our choice to be justified.

The experiments were performed at the insertion-device beamline ID32 at the European Synchrotron Radiation Facility. The sample was illuminated with 8 keV X-rays monochromatized by a Si (1 1 1) double crystal monochromator with a resolution of $\Delta E/E = 1.3 \times 10^{-4}$. The unfocused $1.2 \times 2\,\mathrm{mm}^2$ (vertical × horizontal) X-ray beam was collimated to a size of 0.2 mm × 0.5 mm before reaching the sample. The chosen photon energy of $E = 8$ keV was high enough for the present purpose. The electron signal, decreasing drastically with increasing photon energy, was of good intensity which allowed rapid measurements with good statistics. The samples were mounted side by side on the same sample holder and placed alternatively in the beam at exactly the same position by translation. Thus each sample was

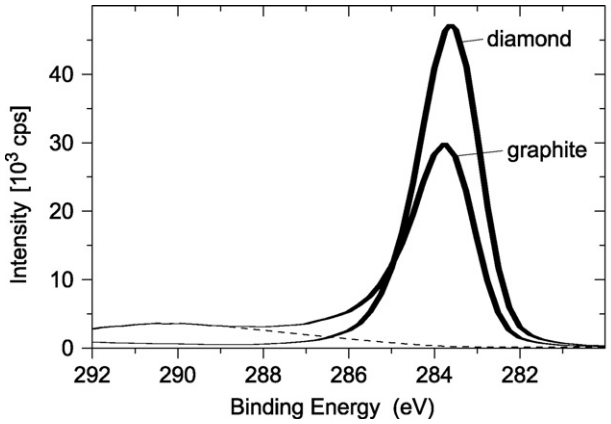

Fig. 2. Elastic C 1s-lines of diamond and graphite, each measured 3 times alternatively and plotted as a function of binding energy. The areas C_{el}^D and C_{el}^G of the lines are taken as representative of the intensities C_n^D and C_m^G in Eq. (4). A background from the onset of energy-loss (dashed line [16]) was subtracted for graphite. The line widths correspond to the maximum deviation of the recorded curves for the three scans for each sample.

measured three times at the C 1s line. The incident beam hit the surface at normal incidence and the spectra were recorded at an electron emission angle of 45° in our experiments. The total time span for all measurements was 100 min during which the intensity from the storage ring dropped by only 1.5%. In this way all extrinsic parameters, such as efficiency of the electron analyzer, photon flux, angle of acceptance, etc. cancel out when comparing the yield from the two samples.

3. Results

Fig. 2 shows the results in the region of the C 1s peak. The envelopes over the three recorded spectra for each sample, are displayed as a function of binding energy. Thus the width of the curves represents the scatter of the measurements. The spectra show a very good reproducibility within <±1% in the intensity maximum. There is only some minimal drift of the monochromator or irreproducibility of the setting of the electron analyzer. Fig. 3 displays the data over a wider range. There we display the spectra on an energy-loss scale (the variable is T) with the zero point at the elastic line (see also Section 4.2). The spectra of diamond and graphite

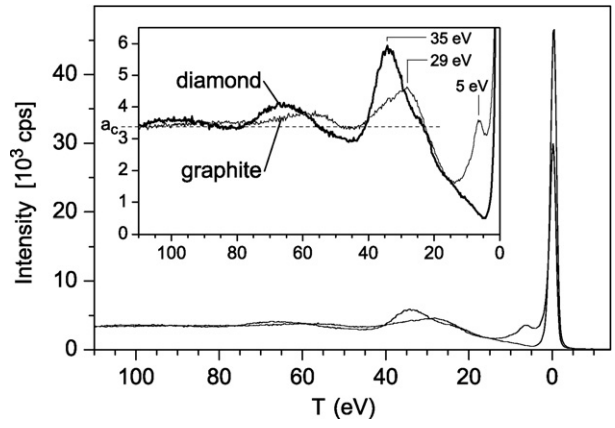

Fig. 3. Wide range C 1s spectrum showing the energy-losses in diamond and graphite next to the main line plotted as a function of energy-loss T relative to the elastic line. For diamond, the energy gap of 5.5 eV shows up as a decrease of intensity right after the elastic peak almost to zero. For graphite, the peak at 5 eV energy-loss originates from inter-band transitions. The inset shows the expanded high-energy parts of the spectra which tend towards a constant intensity a_c being practically the same for diamond and graphite.

are quite different. In the case of diamond the energy gap of 5.5 eV clearly shows up as a decrease of intensity almost to zero right after the elastic peak. In graphite at 5 eV energy-loss a peak originating from inter-band transitions extending up to the Fermi energy can be distinguished.

A line fit program [16] was used for the graphite spectra to separate the elastic line from the peak at $T = 5$ eV. The ambiguity of the line shape results in a small error of a few percent in determining the intensity of the elastic line. As a result we obtain for the ratio of the thus separated and integrated elastic peak areas C_{el} (D for diamond, G for graphite) $C_{el}^D/C_{el}^G = 1.43 \pm 5\%$. This result will be used in Section 4.1.

In Fig. 3 we also note broad, plasmon-like peaks displaced from the elastic peak to higher binding energies or energy-loss by ~35 eV for diamond and ~29 eV for graphite. Indications of the twofold plasmon loss are also discernible, but towards higher loss energies the multiple losses rapidly merge to a structureless constant level of intensity. The single measurable quantity is its amplitude a_c which, within the accuracy of our measurement, happens to be the same for diamond and graphite. This intensity is entirely due to the overlap of consecutive inelastic scattering events exciting either collective modes or individual electrons in the solid. We shall refrain from attempting to isolate plasmon peaks from this "background" as it was attempted in other evaluations. In our evaluation the intensity of this region of overlapping energy-losses relative to that of the elastic peak can profitably be exploited as will be shown in detail in Section 4.4.

4. Photo excitation and electron transport

The photoelectron emission process can be broken down into individual steps, i.e., (1) primary photoabsorption, (2) emission from the atom, where the atom with its core hole including the surrounding solid can be left in its completely screened ground state (elastic line) or in an excited state which gives rise to "intrinsic" losses, (3) transport through the material during which the electron can be scattered elastically or inelastically giving rise to individual or collective excitations such as e.g. plasmons and single-electron excitations, and (4) the transport through the surface of the medium which can give again rise to excitations, in particular surface plasmons.

There are two shortcomings of this four step model, which we like to mention although they will have only a minor influence on our result. Atoms excited very close to the surface are screened differently than those excited in the bulk. This gives rise to specific intrinsic surface losses, but at our high electron energies with IMFPs of the order of 100 Å this gives only a small contribution to our spectra (even at the emission angle of 45° in our experiments). In addition, their excitation will compensate in the overall intensity budget to a large extent the corresponding reduction of intrinsic volume losses for these atoms. The second point is that we neglect interference between intrinsic and extrinsic excitations. In a classical picture interference is best understood the following way. In the initial stage of separation of the electron from the hole the field is a weak dipole field. A dipole field is the classical "interference" of two separate Coulomb fields from two opposite charges. At larger distances the two charges are screened individually. Thus the large mean free path reduces the effect of interference already. Further, quantum mechanical interference can only occur when the final state is the same for two different channels of excitation. Therefore, only those extrinsic losses originating from electrons excited by the elastic line can interfere with the intrinsic losses because only for them will the final state energy be the same. We are going to quantify this fraction of extrinsic losses later and will find that it is <1/2. There is a host of publications on intrinsic excitations and

interference [17–23]. It was already pointed out in Refs. [17–19] that interference becomes weak in the sudden approximation (at high energies).

4.1. Excitation and energy-loss at high kinetic energies

Due to our high primary electron energies, we may assume that the collected electrons have propagated without significant deviations from the direction of acceptance of the lens of the analyzer (being a small cone of 6° opening angle). Thus, we assume that in the first few elastic- and inelastic-scattering processes paths with large angular deviations contribute negligibly. This situation should hold at least for the electrons in the ~110 eV interval of energy-loss of our spectra. The validity of this assumption will be justified further below (see Appendixes A and C).

The elastic C 1s lines are the only features easily discernible in the spectra. They are a part of the primary excited electrons. As a matter of fact, Doniach–Sunjič satellite excitations [24], which are due to rearrangement of states at the Fermi surface, and phonon excitations cannot be separated from the elastic line, but this does not influence our analysis. All electrons (and therefore also those originally in the elastic peak) penetrate the surface only once and only a fixed small fraction of them (<10% at ~8 keV (see Appendix B) undergoes energy-loss due to surface excitations (e.g. surface plasmons). For the interpretation of the intensity of the elastic line alone, we need to know the fractional decrease in intensity due to surface plasmon excitation. But surface loss contributions are small (see Appendix B) and therefore any corrections are of minor importance here. This will be discussed later, while in the following we start with an analysis of the overall intensity of the primary line and single and multiple extrinsic energy-losses.

The integrated count rate in the detector from a particular primary photoelectron emission ($n=0$) or its nth extrinsic energy-loss contribution is given by

$$C_n = N_{ph} \times A_{an} \times \rho_{At} \times \sigma_{in} \times p(\theta,\varphi) \int_0^\infty \mathrm{d}x P_n\left(\frac{x}{\lambda_{in}\cos\alpha}\right), \qquad (1)$$

where N_{ph} is the flux of photons on the sample, A_{an} is the acceptance and efficiency of the electron analyzer (we refrain from analyzing the geometry in detail, since later it will drop out in our relative measurements), ρ_{At} (here ρ_G and ρ_D) is the volume density of atoms giving rise to a particular line, σ_{in} is the sub-shell ionization cross-section (the index stands for "inelastic"), $p(\theta,\varphi)$ is the anisotropy parameter (see below) and λ_{in} is the IMFP of the electrons, which in our case of $\alpha=45°$ escape angle to the surface normal gives rise to the effective escape depth $t_{in}=\lambda_{in}\cos(\alpha)$ and P_n is the probability that an electron, which reaches the surface after having undergone n extrinsic energy-losses, originates from depth x. Since the penetration depth of the X-rays is much larger than λ_{in}, the photoelectron excitation density is constant over the relevant depth and only $P_n(x/t_i)$ depends on x. The IMFP λ_{in} varies only slowly with electron energy and we treat it as constant considering the small variation of T compared to the initial energy $E=7716$ eV. Thus, P_n is given by the Poisson distribution

$$P_n\left(\frac{x}{t_{in}}\right) = \frac{(x/t_{in})^n}{n!}\ \exp\left(\frac{-x}{t_{in}}\right) \qquad (2)$$

Then

$$\int \mathrm{d}x P n\left(\frac{x}{t_{in}}\right) = t_{in} = \lambda_{in}\ \cos(\alpha) \qquad (3)$$

is valid for all n. Thus according to Eq. (1) the yields C_n of electrons which have encountered zero (the primary line) or n extrinsic energy-losses are all the same.

The angular anisotropy of the photoemission process [25] is taken into account by the correction factor $p(\theta,\varphi)$ for an electron emitted in the direction of the spectrometer, which is described by angles θ and φ relative to the polarization and propagation directions, respectively, of the incident photon (see e.g. Fig. 3 of Ref. [14]). In our case $\theta=45°$ and $\varphi=180°$. For 8 keV photons $p=0.78$ with the parameters taken from Refs. [26,27]. However, since it is an atomic property it cancels out when comparing diamond to graphite. The fact that it is close to the isotropic average $p=1$ is helpful for our method of analysis in case different elastic-scattering probabilities in the two materials would cause differences in the small but relevant angular deviations from the reference direction.

In comparing the spectral intensities of diamond (D) to those of graphite (G), we eliminate the unknown but constant geometrical factors. In addition the atomic ionization cross-section and the asymmetry parameter are the same and cancel out as well. Thus we obtain:

$$\frac{\lambda_{in}^D}{\lambda_{in}^G} = \frac{\rho_{At}^G}{\rho_{At}^D} \times \frac{C_n^D}{C_m^G}. \qquad (4)$$

While this is valid for the few orders of loss n (for diamond) and m (for graphite), which we consider, it is impossible to distinguish in the spectra the contributions originating from consecutive energy-losses, n, $m \geq 0$ since they rapidly merge into a featureless background. Determination of the intensities ($n=m=0$) of the primarily emitted 1s photoelectrons (primary spectrum) is also not possible since it would require knowledge of the intrinsic part. However, we can calculate C_0^D/C_0^G under the assumption (as we did in a previous investigation [14]) that C_{el} (the integral intensity of the elastic line) is a material-independent constant fraction of C_0. Thus, when inserting into Eq. (4) $C_0^D/C_0^G = C_{el}^D/C_{el}^G = 1.43 \pm 5\%$ from Fig. 2 and $\rho_D/\rho_G = 1.54$ we obtain $\lambda_{in}^D/\lambda_{in}^G = 0.93$ (Table 1). We reiterate that this result is obtained under the additional assumption that surface losses reduce the intensity of the elastic line by the same fraction in both materials.

4.2. Energy-loss spectra

The total electron spectrum consists of the primary spectrum and electrons which experience subsequent extrinsic energy-losses, due to collective and single-electron excitations, while traversing the material. In addition, all electrons (elastic and inelastic) excite surface modes while escaping through the surface. As can be seen in the spectra of Fig. 3, a practically constant intensity distribution is produced after about just two to three consecutive energy-losses. There is, however, useful information contained in the magnitude a_c of this background resulting from the overlapping multiple energy-losses.

We denote the energy-loss distribution function of an electron of kinetic energy E losing energy T in an extrinsic process as $w(E,T)$

Table 1
Parameters and IMFPs for diamond (D) and graphite (G). ρ_{At} = atomic density, T_p = plasma energy, T_1 = oscillator in Eq. (18), C_{el} = intensity elastic peak, λ_{in} = IMFP.

1	2	3	4	5	6	7	8
	ρ_{At} (10^{28}/m^3)	T_p (eV)	T_1 (see Eq. (18))	C_{el} (from Fig. 2)	C_{el} (from λ_{in})	λ_{in} (see Eq. (19))	λ_{in} (after [9])
D	17.6	31.2	36.7			91.4	96.8
G	11.4	24.9	24.9			92.1	96.1
D/G	1.54			$1.43 \pm 5\%$	0.93	0.99	1.01

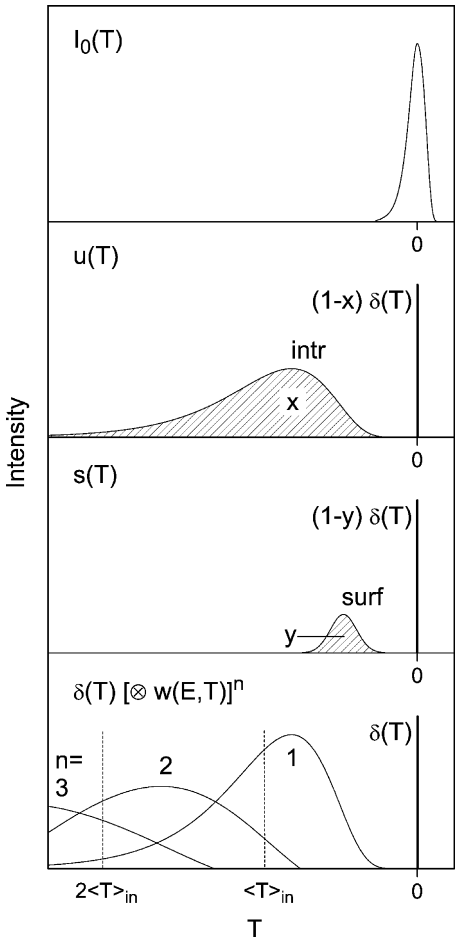

Fig. 4. Schematic contributions to the different processes contributing to the overall energy-loss spectrum (see Eqs. (7) and (8)). $I_0(T)$ is the excitation spectrum including energy spread of the exciting photons, core hole life-time width, phonon excitations and Doniach-Sunjič [24] excitations; $u(T)$ is the complete primary emission spectrum with elastic $(1-x)$ and intrinsic (x) contributions; $s(T)$ is the surface loss spectrum (including the $(1-y)$ no-loss line) producing surface losses with probability y (see Appendix B); $w(E,T)$ $(n=1)$ is the extrinsic energy-loss distribution with its multiple losses $(n=2, 3\ldots)$ obtained by convolution. The δ-function corresponds to escape without extrinsic loss. The overall spectrum will then be obtained as the convolution of all four contributions

where E is the kinetic energy of the electrons and T the energy-loss. As a probability distribution it is normalized

$$\int_0^E w(E,T)\mathrm{d}T = 1. \tag{5}$$

The mean extrinsic energy-loss is given by

$$\langle T\rangle_{in} = \int_0^E Tw(E,T)\mathrm{d}T. \tag{6}$$

In order to illustrate the following procedure schematically we refer to Fig. 4. We consider the overall spectral intensity generated by a series of convolutions of different functions, where the first three in Fig. 4 concern processes which occur only once. These result in a spectral function $I(T)$ which is the primary spectrum including surface losses. $I(T)$ is generated in the following way:

$$I(T) = I_0(T)\otimes u(T)\otimes s(T). \tag{7}$$

Here $I_0(T)$ is a narrow line whose intensity is determined by Eq. (1) primarily by the cross-section σ, the density of atoms ρ_{At} and the number of impinging photons before any secondary processes occur. Photon density and collection efficiency of our electron analyzer can be considered as a common scale factor to all our measurements and does not need to be known. For practical reasons we include in $I_0(T)$ broadening due to the energy width of the exciting photons, the resolution function of the electron analyzer, the core-level life time (eventually the Doniach–Sunjič profile [24]) and phonon broadening. The distribution $u(T)$ represents the primary distribution of electrons as emitted at the site of the atom. It consists of a zero loss δ-function elastic line and, separated from the elastic line, all the satellite structures due to the incomplete screening of the core hole (intrinsic losses).

The commutability of convolutions allows us to include the excitation of extrinsic surface modes $s(T)$ here although actually in the chain of events it is the final process. It consists of a no-loss δ-function line and the inelastic surface loss spectrum. Because it is an extrinsic process it does not belong to the primary line. But again each electron is penetrating the surface only once and thus subject to this process only once. Even if we could excite multiple surface losses at grazing incidence this would not matter and would completely be included in a single probability distribution function $s(T)$. Here $s(T)$ consists of a no-loss δ-function line and the inelastic surface loss spectrum of weight $y=0.07$ (see Appendix B). Both probability distributions $u(T)$ and $s(T)$ are normalized to unity and thus do not alter the integrated intensity of $I_0(T)$, they only spread it out on the energy-loss scale T.

Since E is much larger than $\langle T\rangle_{in}$ it is safe to consider not only λ_{in} but also the shape of $w(E,T)$ as having negligible E-dependence [6]. Thus E is a fixed parameter in the following and we obtain the overall intensity spectrum as

$$\begin{aligned} I_{tot}(T) &= I(T) + I(T)\otimes w(E,T) + I(T)\otimes w(E,T)\otimes w(E,T) + \ldots \\ &= \sum_{n=0} I(T)\otimes\delta(T)(\otimes w(E,T))^n \end{aligned} \tag{8}$$

With the normalization of $w(E,T)$ (see Eq. (5)) Eq. (8) is consistent with Eq. (3) which gives equal weight to all orders n of energy-loss in our experimental geometry. Note that the δ-function in the last term is obsolete here, but we need it to be consistent with Fig. 4, where we show the convolutions of Eqs. (7) and (8) separated into their individual components.

According to the theory of convolution, the mean of the nth convolution is $n\times\langle T\rangle_{in}$ and is shifted relative to the mean

$$\langle T\rangle_I = \frac{\int I(T)T\mathrm{d}T}{\int I(T)\mathrm{d}T} \tag{9}$$

of $I(T)$ by this amount. $\langle T\rangle_I$ can be considered as a natural energy reference for all extrinsic losses such that the mean of the nth energy-loss is $\langle T\rangle_I + n\times\langle T\rangle_{in}$. It is, however, *a priori* not possible to determine $\langle T\rangle_I$ on the energy-loss scale in our spectra. The theory of convolutions gives the additional result that the mean square deviation from $\langle T\rangle_I + n\times\langle T\rangle_{in}$ is proportional to n so that broadening is proportional to $\sqrt{n}$.

The successive convolutions place increasingly broadened distributions of equal weight along the T-axis. These broaden and merge into a continuum with constant amplitude a_c. There has to exist a ΔT such that

$$a_c\times\Delta T = C_n = C_0 = \int I(T)\mathrm{d}T. \tag{10}$$

It is tempting to set $\Delta T = \langle T\rangle_{in}$ and to claim that the distributions are placed equidistantly on the T-axis. While this appears intuitively correct, caution is advised. It is not clear whether the mean of a distribution, the median, or something else should be taken as the center of the respective spectral weight which due to overlap leads to a final smeared constant background. For symmetric distributions, the mean (center of "gravity") is equal to the median (dividing line where equal integrated intensities are on both sides). For

asymmetric distributions, the median deviates from the mean. We therefore performed model calculations with several types of realistic asymmetric model distributions (having a tail towards large T) which showed that (1) the multiple losses rapidly merge into a background of amplitude a_c which satisfies Eq. (10) with $\Delta T = \langle T\rangle_{in}$, (2) the separation of successive medians converges rapidly to $\langle T\rangle_{in}$, but (3) the positions of the medians may deviate from $\langle T\rangle_I + n \times \langle T\rangle_{in}$, but the deviation will be less than $\langle T\rangle_{in}/2$. Because of (1) we proceed applying $\Delta T = \langle T\rangle_{in}$. We need then to know $\langle T\rangle_{in}$ in order to determine the C_n from Eq. (10).

4.3. Extrinsic inelastic scattering

In order to estimate $\langle T\rangle_{in}$ we need to know the energy-loss probability distribution integrated over all allowed momentum transfers. The starting point is the same as that usually applied to calculate the IMFP see, e.g. [6]. The probability per unit path length for an electron with energy E to undergo an energy-loss T in an interval dT is

$$W(E,T) = \frac{1}{\pi a_0 E}\int_{q_-}^{q_+}\frac{\mathrm{d}q}{q}\,\mathrm{Im}\frac{-1}{\varepsilon(q,T)}, \tag{11}$$

where a_0 is the Bohr radius, Im$[-1/\varepsilon(q,T)]$ is the imaginary part of the complete dielectric constant, the so-called energy-loss function, depending on momentum transfer $\hbar q$ in the energy-loss process and on T; q is limited due to kinematics [6] to the region between q_- and q_+, with

$$q_\pm = \sqrt{\frac{2m}{\hbar^2}}(\sqrt{E} \pm \sqrt{E-T}). \tag{12}$$

In integrating over all allowed energy-losses we obtain the inverse IMFP

$$\lambda_{in}^{-1} = \int_0^E \mathrm{d}T W(E,T). \tag{13}$$

The normalized distribution function of energy-losses already introduced above in Eq. (5) is then

$$w(E,T) = \lambda_{in} \times W(E,T). \tag{14}$$

This function often displays structural similarities to the so-called optical energy-loss function Im$[-1/\varepsilon(0,T)]$, but it is different due to dispersion (q-dependence) and angular (q-) integration as shown in detail below and in Appendix A.

For momentum transfers much smaller than $q_c = 2\pi/r_s$ where r_s is roughly the inter-electron separation ($r_s \sim 1$ Å in our case), Im$[-1/\varepsilon(q,T)]$ describes a predominantly collective response of the material. For $q > q_c$ electron–electron scattering sets in with well defined kinematics. This is characterized in the q–T-plane by the so-called Bethe ridge (see e.g. [28]) such that Im$[-1/\varepsilon(q,T)] \neq 0$ holds for large q only in the vicinity of $T = q^2/2m$. We apply here a model due to Ashley [12] which extrapolates the optical energy-loss function Im$[-1/\varepsilon(0,T)]$ to finite q and generates a smooth transition from e.g. the plasmon dispersion to the Bethe ridge. This model correctly reproduces all the features we need. We neglect exchange effects (as e.g. in Ref. [8]). This is justified by our high electron energies. The details of the derivation are given in Appendix A. We obtain

$$\lambda_{in}^{-1} = \frac{1}{2\pi a_0 E}\int dT'\ \mathrm{Im}\frac{-1}{\varepsilon(0,T')}\ln\frac{4E}{T'} \tag{15}$$

and

$$\langle T\rangle_{in} = \frac{\lambda_{in}}{2\pi a_0 E}\int dT'\ \mathrm{Im}\frac{-1}{\varepsilon(0,T')}T'\,2\ln\frac{2E}{T'}, \tag{16}$$

while Im$[-1/\varepsilon(0,T')]$ has to obey the sum rule

$$\int dT' \mathrm{Im}\frac{-1}{\varepsilon(0,T')}T' = \frac{\pi}{2}T_p^2. \tag{17}$$

T_p^2 is proportional to the density of the four valence-electrons/atom (T_p is the bulk plasmon energy). This requires making use of a *partial* sum rule in Eq. (17) where the upper limit of the integral is the onset of the shallowest core transitions. Correctly, only universal sum rules are valid where the upper boundary of integration is infinity and T_p is determined by the total electron density. For specific materials, however, as there are diamond, graphite and several free-electron metals, like Li, Al, Mg, where there is a large binding energy separation of the valence electrons to the shallowest core levels, the partial sum rule of Eq. (17) is a viable concept. Even there the effective number of valence electrons may be somewhat smaller than the actual number and needs to be determined from optical data. In our case, the possibility to use the actual valence electron density in Eq. (17) and to neglect core electrons altogether in calculating λ_{in} from Eq. (15) is a consequence of the high C 1s binding energy of 284 eV in conjunction with the universal sum rule. The possibility to neglect core electrons in calculating $\langle T\rangle_{in}$ from Eq. (16) needs more attention and is justified here by the fact that the region of our analysis is confined to $T < 110$ eV, a region way below that where core electrons are excited.

We note that the integral term in (16) is only marginally determined by the spectral features of Im$[-1/\varepsilon(0,T')]$. This is a consequence of the sum rule (17), the integrand being modified only by the slowly varying logarithmic term in (16). The major influence on $\langle T\rangle_{in}$ is through λ_{in}. This prompted us to represent the whole Im$[-1/\varepsilon(0,T')]$ function by a single δ-function centred at T_1, whose weight is constrained by the sum rule (17):

$$\mathrm{Im}\left[\frac{-1}{\varepsilon(0,T')}\right] = \frac{\pi}{2}T_p\frac{T_p}{T_1}\delta(T'-T_1). \tag{18}$$

With (18) we obtain from (15)

$$\lambda_{in}^{-1} = \frac{T_p}{4a_0E}\frac{T_p}{T_1}\ln\frac{4E}{T_1}, \tag{19}$$

and from (16)

$$\langle T\rangle_{in} = 2T_1\frac{\ln 2E/T_1}{\ln 4E/T_1}. \tag{20}$$

Tentatively we set in (19) now $T_1 = T_p$, which for graphite yields $\lambda_{in}^G = 92.1$ Å ($T_p = 24.9$ eV) and for diamond $\lambda_{in}^D = 75.9$ Å ($T_p = 31.2$ eV). For diamond, however, there must be $T_1 > T_p$ since, with a band gap of 5.5 eV, spectral weight is missing at low energies. Therefore spectral weight will move to higher energies. If we add the gap energy linearly to T_p we obtain $T_1 = 36.7$ eV yielding $\lambda_{in}^D = 91.4$ Å. Thus, with this simple model (Eqs. (18)–(20)) we obtain $\lambda_{in}^D/\lambda_{in}^G = 0.99$ and confirm within 6% the result $\lambda_{in}^D/\lambda_{in}^G = 0.93$ obtained in Section 4.1 from the ratio of the elastic lines under the assumption that the elastic lines have the same proportion of the primary contribution for both materials. We note in passing that the effect of the band gap in diamond to reduce the efficiency of the valence electrons on λ_{in}^{-1} is in essence the same which renders core-electron scattering unimportant.

Tanuma et al. [4] have analyzed the mean free paths of many materials from 50 eV up to 2000 eV. In their attempts to combine the results into a universal modified Bethe equation they noted more recently [9] that graphite and diamond did not fit well into their scheme. They re-analyzed these materials with better optical constants using a method developed by Penn [11] quite similar to that of Ashley [12]. Their analysis, however, takes into account the full shape of Im$[-1/\varepsilon(0,T')]$. We insert their parameters "β(opt)" (corresponding to the fits at the high-energy end of their analysis

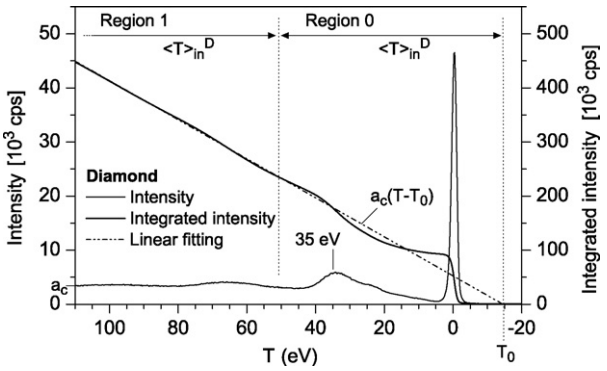

Fig. 5. The integral of the diamond energy distribution as a function of T. A linear fit to the integral at large T is shown as a dash-dotted line. T_0 is the intersection point of the integral with the abscissa. If all structures were smeared out to the average amplitude a_c at high energies the spectrum would start with a step at T_0. Regions of widths $\Delta T^D = \langle T\rangle_{in}^D$ marked on the energy scale would then correspond to the contributions C_n, $n = 0, 1, 2, 3, \ldots$ (see Eqs. (1) and (9)). Also marked is the energy of the "plasmon peak". Note that it neither has to have the position of the plasmon energy T_p nor is its position that of the mean energy-loss $\langle T\rangle_{in}$ according to Eq. (6).

close to 2000 eV) into their modified Bethe equation and obtain $\lambda_i^G = 96.1$ Å and $\lambda_{in}^D = 96.8$ Å for $E = 7716$ eV. These values confirm perfectly the essential equality of the IMFPs in graphite and diamond and, moreover, the absolute values of our model Eq. (19) for λ_{in} to within 5%. The latter result is especially noteworthy given the simplicity of our approach. All values are summarized in Table 1.

4.4. Intrinsic contributions

In Figs. 5 and 6 we show the integrated intensities from T to 110 eV as a function of the lower boundary T of the integral for diamond and graphite, respectively. At the high-energy-loss end the integrated intensity rises linearly due to the constant intensity a_c in the spectra. The linear fit (dash-dotted line), which has the same slope for diamond and graphite, serves to find the energy T_0. At T_0 the spectra would begin if all the structures in the spectra were smeared out to the constant level a_c. The values are $T_0^D = -14.5$ eV for diamond (Fig. 5) and $T_0^G = -11.7$ eV for graphite.

The interval covering the contribution C_0 (Eq. (10)) of the primary excitation starts at T_0 and like those of the following contributions C_n is of length $\langle T\rangle_{in}$. To repeat: the constancy of intensity a_c at the high-energy end together with our model calculations allows us to set at high energies $\Delta T = \langle T\rangle_{in}$ in Eq. (10). Once this is done, ΔT is fixed for all orders n of energy-loss down to $n = 0$. Each interval

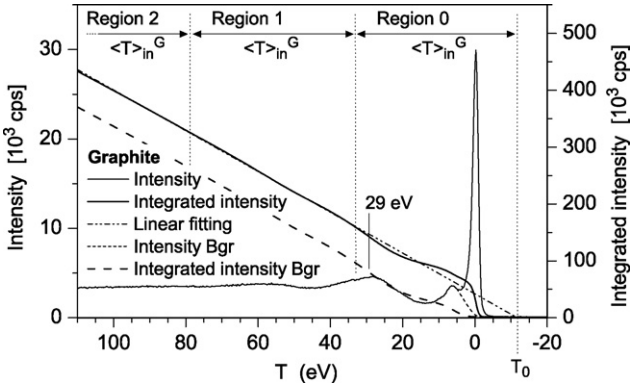

Fig. 6. The integral of the graphite energy distribution as a function of T. Also the integral over the subtracted "background" according to Fig. 2 is shown as a dashed line. For the other symbols and spectra see caption of Fig. 5.

has its virtual center at

$$T_C(n) = T_0 + \left(n + \frac{1}{2}\right) \times \langle T\rangle_{in}. \tag{21}$$

Centering in this way has no other meaning than covering the contributions C_n for $n = 0, 1, 2, 3, \ldots$ one after another with a continuum amplitude a_c obtained at large T. In principle, the exact position of T_0 and thus that of $T_C(0)$ is completely irrelevant for our analysis. With model calculations, however, we nevertheless wanted to understand its relationship with the position of $\langle T\rangle_I$ according to Eq. (9), where the primary intensity would be centered if one could isolate it from overlap. What determines the position of T_0 is a process occurring at larger n in a way not easy to determine, especially with overlapping asymmetric probability distributions $w(E,T)$ not known in detail. Model calculations with simple asymmetric functions $w(E,T)$ (having a long tail to higher energies T) showed that $0 < \langle T\rangle_I - T_C(0) < \langle T\rangle_{in}/2$. In Section 4.5 we shall come back to this question and will try to estimate $\langle T\rangle_I - T_C(0)$ from our data in order to see if it stays within these limits. This is an exercise to add confidence in our detailed understanding of the generation of the continuum at large T.

The elastic peaks at $T = 0$ correspond to the steps of magnitude C_{el}^D and C_{el}^G in the graphs of the integrated intensities in Figs. 5 and 6. Their ratio has already been determined from Fig. 2 in Section 3. If smeared to the level a_c according to $C_{el} = a_c \times \Delta T_{el}$ these would correspond then to intervals $\Delta T_{el}^D = 25.7$ eV for diamond and $\Delta T_{el}^G = 18$ eV for graphite. It is obvious that the ΔT_{el} cannot exhaust the full ΔT from Eq. (10), which would require $\Delta T_{el} = \langle T\rangle_{in}$ which is larger than T_p (according to (20) with $T_1 \approx T_p$). This contradicts evidence from the broad "plasmon" peaks (see Fig. 3) at ~35 eV for diamond and at ~29 eV for graphite which allow at least for a rough estimate of the plasmon energies T_p. We realize here already qualitatively that there need to be appreciable intrinsic contributions to the primary intensities in addition to the elastic peaks.

Introducing now in Eq. (20) those values for T_1, which have produced very reasonable values for λ_{in}^D and λ_{in}^G we obtain $\langle T\rangle_{in}^D = 65.8$ eV and $\langle T\rangle_{in}^G = 45.0$ eV. Since all the intensities have to be the same $C_0 = C_1 = C_2 = \ldots + C_n$ we obtain from Eqs. (10) and (4) $\lambda_{in}^D/\lambda_{in}^G = (\langle T\rangle_{in}^D/\langle T\rangle_{in}^G) \times (\rho_{At}^G/\rho_{At}^D) = 0.95$ in close agreement with the value derived from the ratio of the elastic peak intensities.

This becomes evident when determining now the intrinsic contributions. We can write in terms of the equivalent energy intervals

$$\frac{C_{el}}{C_o} = \frac{\Delta T_{el}}{\langle T\rangle_{in}} \tag{22}$$

and obtain $C_{el}^D/C_0^D = 0.39$ and $C_{el}^G/C_0^G = 0.40$. Within the accuracy, with which we (and Tanuma et al. [9]) have determined the parameters defining $\langle T\rangle_{in}$, the fractions of the elastic contributions to C_0 (and thus, also the complements, the intrinsic contributions) are practically the same for both materials. This justifies in retrospect our simple evaluation of the relative $\lambda_{in}^D/\lambda_{in}^G$ values from the elastic lines alone in Section 4.1. Surface losses have no effect on the integral primary loss C_0 as a whole since they cause only a redistribution of intensity. But they have diminished the integral intensities of the elastic peaks by 7% (see Appendix B), for which a correction is needed. Thus the true elastic intensity C'_{el} is 42% and intrinsic losses C_{int} are 58% of the total primary excitation process C_0 for diamond, and 43% and 57%, respectively, for graphite. The results are summarized in Table 2.

These results are astonishing on first sight since screening of the hole and thus intrinsic losses should differ considerably between an insulator and a semimetal. At second sight, however, one has obviously to differentiate here between static and dynamic screening. The sudden creation of the hole acts on the material in the same way as the fast moving electron, thus resulting in the same mechanism and almost the same spectra for intrinsic and extrinsic

Table 2
Intrinsic and extrinsic losses and IMFPs. $\langle T\rangle_{in}$ = mean extrinsic loss, Col. 3: C_0 is proportional to $\langle T\rangle_{in}$ (after Eq. (10)), ΔT_{el} = elastic loss equivalent, C'_{el} = elastic intensity corrected for surface losses, C_0 = total primary intensity, C_{intr} = intrinsic intensity.

1	2	3	4	5	6	7
	$\langle T\rangle_{in}$ (see Eq. (20))	λ_{in} (from Col.2)	ΔT_{el} (from Figs. 5 and 6)	$C_{el}/C_0 = \Delta T_{el}/\langle T\rangle_{in}$	$C'_{el}/C_0(C_{el}\text{corr})$	C_{intr}/C_0
D	65.8		25.7	0.39	0.42	0.58
G	45.0		18.0	0.40	0.43	0.57
D/G	1.46	0.95	1.43	0.98	0.98	

excitations. Also in a good metal like aluminum the intrinsic energy-loss leads to a peak at the plasmon energy. The dynamic metallic response at the Fermi energy manifests itself in the Doniach–Sunjič [24] excitations, which, however, is included in the elastic line.

Note that our method provided these values from a very simple analysis of the amplitude of overlapping contributions without the need to disentangle the individual components except that of the elastic peak. Several authors (see e.g. [21–23]) prefer to give the ratio as intrinsic/extrinsic at the position of overlapping first plasmon peaks. What they understand as "extrinsic" is different from our terminology. We do not want to go into the details of how these two contributions and multiple extrinsic energy-losses were separated by them. In their terminology our C_{int} would more or less represent the intrinsic plasmon. However, only those extrinsic plasmons which are excited by the elastic peak have an overlap with the intrinsic ones. Their intensity is equal to C'_{el} (C_{el} corrected for surface losses) since only that part of the convolution of $w(E,T)$ with the "primary" intensity $I(T)$ in Eq. (8) which convolutes with the elastic line superimposes at the first plasmon position. Thus $C_{\text{int}}/C'_{el} \approx 1.35$ would be our result in their terminology. Yubero and Tougaard [21] obtained 0.65 for the intrinsic/extrinsic ratio for the Al 2s excitation with 1130 eV kinetic energy, a value roughly half of our result, however, in a different energy range with a different material and another evaluation procedure. At this moment we are not aware of any results in the literature for materials similar to ours.

4.5. Overview of all contributions to I(T)

It is helpful to look at our spectra (Fig. 3) again from the point of view of the generation of the primary distribution $I(T)$ (including surface excitations $s(T)$) from consecutive convolutions according to Eq. (7) and Fig. 4. We visualize in Fig. 7 how we determine $\langle T\rangle_I$ taking diamond as the example. We are only able to locate the mean $\langle T\rangle_I$ of $I(T)$ (Eqs. (7) and (9)) and not the function $I(T)$ itself because $I(T)$ and the extrinsic components are superimposed in the experimental spectra. The intrinsic part in Fig. 7 is therefore only a rough sketch of how it may look. Its details, however, are not known and need not to be known for the calculation of $\langle T\rangle_I$ from the means of its constituents.

We consider for our present analysis the total intensity to be normalized to unity ($a_c \times \langle T\rangle_{in} = C_n = 1$ in Eq (10)). The mean is obtained as the sum of the means of all individual contributions. We start with diamond. The elastic line contributes $0 \times (0.42–0.03) = 0$. The value 0.42 stands for the primary elastic line; it has to be reduced by 7% for the subsequent excitation of surface losses. Being aware that surface losses are typically located at around 0.7 the "bulk plasmon" peak position (here 35 eV) we attribute to the surface loss originating from the elastic line a contribution of 24.5×0.03. Next the contribution from the intrinsic losses has to be estimated. We assume here (in a reasonable approximation) that intrinsic and extrinsic losses have similar shapes. Intrinsic losses then have a mean energy at a separation of $\langle T\rangle^D_{in}$ from the position of the elastic line. This leads to a moment of $\langle T\rangle^D_{in} \times (0.58 - 0.04)$. The 0.04 term stems again from the 7% reduction due to surface excitation and reappears as a moment of $(\langle T\rangle^D_{in} + 24.5) \times 0.04$. We sum up all the moments and obtain for the position of $\langle T\rangle^D_I$

$$\langle T\rangle^D_I = (\langle T\rangle^D_{in} \times 0.58) + (24.5 \times 0.07). \tag{23}$$

With $\langle T\rangle^D_{in} = 65.8$ eV we obtain $\langle T\rangle^D_I = 39.9$ eV for diamond. Introducing for graphite $\langle T\rangle^G_{in} = 45$ eV and 20.3 eV for the surface loss energy we obtain $\langle T\rangle^G_I = 27.0$ eV.

As we noted already in Section 4.4 following the discussion of Eq. (21) the position of $\langle T\rangle_I$ differs from that of $T_C(0)$, the virtual positions of the centers of "Region 0" in Figs. 5 and 6. In that case we obtained $T^D_C(0) = 18.4$ eV and $T^G_C(0) = 10.8$ eV. As we mentioned above, our model calculations with asymmetric energy-loss distributions $w(E,T)$ showed that the shift $\Delta = \langle T\rangle_I - T_C(0)$ should be less than $\langle T\rangle_{in}/2$, as indeed it is in both cases. For diamond, we find a shift of $\Delta^D = 21.5$ eV compared to $\langle T\rangle^D_{in}/2 = 32.9$ eV. For graphite the shift is $\Delta^G = 16.2$ eV compared to $\langle T\rangle^G_{in}/2 = 22.5$ eV. The results are summarized in Table 3.

From an intuitive point of view it is difficult to accept that the mean of $w(E,T)$, the mean first extrinsic energy-loss, is shifted from the elastic line to an energy $\langle T\rangle_I + \langle T\rangle_{in}$, which lies well above the "plasmon" peaks in the spectra. This, however, is understood in looking at Eq. (26) in Appendix A, which shows that $w(E,T)$ falls off at high energies T as T^{-2} and thus the integrand in calculating $\langle T\rangle_{in}$ falls off as T^{-1}. This integral would diverge if T was not limited by $T \le E$. Already Bethe in his seminal paper [10] noted in his atomic calculations that about half of the energy (here T) is transferred to fast secondary electrons. In this asymmetric function as we mentioned already at the end of Section 4.2, the mean gives much

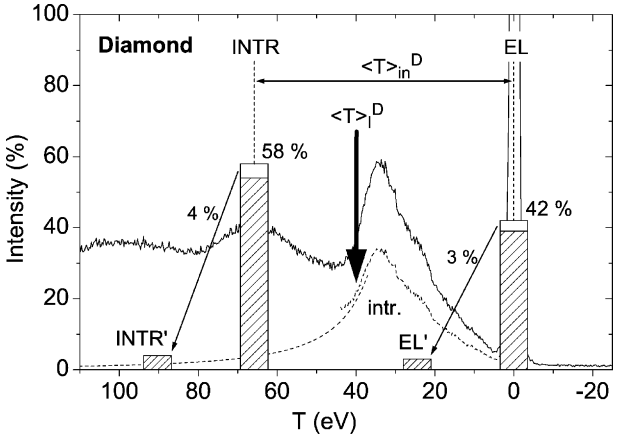

Fig. 7. Determination of the position of the mean $\langle T\rangle_I$ of the primary distribution for diamond according to Section 4.5. This figure visualizes for diamond the individual convolutions shown in Fig. 4. The intrinsic contribution cannot be separated from the overall spectrum. But it can be visualized approximately (intr.) as a ~58% copy of the energy-loss region up to the first peak and a $c/(T-b)^2$ tail to the higher T-region with appropriate constants c and b. The actual shape is not relevant for the determination of $\langle T\rangle_I$. The only approximation made is that the intrinsic and extrinsic spectra have similar shapes. The individual contributions (elastic (EL), intrinsic (INTR), with surface losses (EL′, INTR′)) are shown with their relative weight as columns at the mean positions determined from our analysis (see Section 4.5). $\langle T\rangle_I$ is then the mean of the individual means according to Eq. (21) and Tables 2 and 3.

Table 3
Consistency check for the shift Δ of $T_0 + \langle T\rangle_{in}/2$ relative to the mean of the primary distribution including surface losses $\langle T\rangle_I$ (see also Fig. 7), T_0 is taken from the extrapolations in Figs. 5 and 6.

1	2	3	4	5	6
	T_0 (from Figs. 5 and 6)	$\langle T\rangle_{in}/2$ (eV)	$\langle T\rangle_I$ (from (25))	$T(0) = T_0 + \langle T\rangle_{in}/2$ (from (21))	Δ (from Cols. 4,5)
D	−14.5	32.9	39.9	18.4	21.5
G	−11.7	22.5	27.0	10.8	16.2

weight to the long high-energy tail. If we were only interested in the distribution of spectral density, a quantity like e.g. the median would be more appropriate. Then the integral over the spectral density $w(E,T)$, which in essence determines $1/\lambda_{in}$, converges well even if the upper boundary was infinity and the median of $I(T)$ comes to lie at lower energy.

In the analysis of the succession of multiple energy-losses, the mean $\langle T\rangle_{in}$ rather than the median or any other quantity allows evaluation of the spectra in a mathematically simple form. The sequence of multiple "plasmon" peaks, for example, as they show up especially in a free-electron metal like Al (see e.g. [23]) convey the feeling that their separation would represent the frequency of contributions of equal weight to the spectrum. But we have to consider $w(E,T)$ there as a sum of two parts, the peak-term and the dispersed high-energy "tail"-term. It is easily shown that in repeated convolutions the peak will broaden and repeat with the period of its loss energy superimposed on an increasing "background" originating from the "tail"-term.

5. Summary and outlook

We have measured the excitation spectra of the C 1s level excited by 8 keV photons over a range of ∼100 eV in diamond and graphite. This is an energy range in which intrinsic, extrinsic and surface energy-losses overlap and merge. Nevertheless we were able to extract from the spectra the information on the intrinsic contributions and the IMFPs.

Diamond has a density 1.54 times that of graphite. In spite of this large difference, the IMFPs for the 7716 eV photoelectrons are practically the same in agreement with calculations of Tanuma et al. [9] for much lower energies determined from optical constants. Evaluation of the ratio of the integrated intensities of the elastic lines gives $\lambda_{in}^D/\lambda_{in}^G = 0.93 \pm 5\%$ and correcting for the small difference in intrinsic contributions gives $\lambda_{in}^D/\lambda_{in}^G = 0.95$. With the parameters used in the equations deduced from Ashley's model [12] we obtain $\lambda_{in}^D = 91.4$ Å and $\lambda_{in}^G = 91.1$ Å while the extrapolation from the values of Tanuma et al. [9] gives $\lambda_{in}^D = 96.8$ Å and $\lambda_{in}^G = 96.1$ Å, all in very good agreement. The fact that the two materials with an electron density ratio of 1.54 nevertheless have the same IMFPs is explained by the fact that the energy gap in diamond pushes oscillator strength to higher energy which reduces its effectiveness in the energy-loss function.

From the continuum level at which multiple extrinsic energy-losses merge we find for both diamond and graphite that the elastic line (that leaving the 1s hole completely screened, i.e., in its lowest excited state) is only 42% and 43%, respectively, of the primary excitation. The remaining fraction, 58% for diamond and 57% for graphite, is exciting intrinsic energy-losses (those due to incomplete screening of the hole charge). At first sight, a value of almost 60% for intrinsic excitations may appear large but one should not forget that for our high X-ray energies the sudden approximation is valid. Intrinsic losses are only a special class of satellite structures and there are sufficient examples in the literature where satellite lines dominate the spectra and the well screened hole-state almost disappears. Here we deal mainly with an extra-atomic hole-screening due to the surrounding medium.

Further, the equality of the intrinsic fractions in diamond and graphite was unexpected since hole-screening should differ in a semimetal from that in an insulator. The clue is that dynamical screening is the process which matters here. This is governed by the same energy-loss function which determines also the IMFPs while the dynamic contribution from the metallic character of graphite is manifest in the Doniach–Sunjič [24] line shape. This is, however, in our evaluation included in the elastic line. Our results and the relevant parameters are summarized in Table 2.

Our method of evaluating the continuum to which multiple energy-losses merge is likely to be of more general interest. It will, hopefully, be applicable also to other materials. At the kinetic energies of high-energy X-ray photo emission spectroscopy (HAXPES) we are in a regime where a quasi-unidirectional electron trajectory is a good approximation. This situation leads to a simple one-dimensional model of consecutive inelastic events. This approximation is valid as long as the number of inelastic scattering events is not too large and if large-angle elastic scattering can be neglected (see Appendix C). The spectral region for which our analysis is applicable will be material dependent. A simple analysis allows interpretation of the constant intensity to which the first few characteristic energy-losses rapidly merge. The additional information needed is the mean energy-loss $\langle T\rangle_{in}$ taken over all momentum transfers (which translates into an average over all the allowed relevant scattering angles). In the determination of $\langle T\rangle_{in}$ we profited indirectly from the IMFP analysis at lower energies of Tanuma et al. [9]. $\langle T\rangle_{in}$ can be determined directly from optical constants making use of the simple equation (16). As for diamond and graphite it should be possible also for other materials to approximate $\langle T\rangle_{in}$ with the help of sum rules (see Eqs. (18)–(20)). We hope that this method will contribute to a better appreciation of the information otherwise usually ignored as "background".

Acknowledgements

We thank Malvina Trzhaskovskaya for providing asymmetry parameter values individually calculated for specific energies.

Appendix A. Derivation of $W(E,T)$ from the Ashley model

Here we proceed from Eq. (11) with the following reasonable model function due to Ashley [12] which serves to extrapolate the optical energy-loss function into the $q > 0$ regime:

$$\mathrm{Im}\frac{-1}{\varepsilon(q,T)} = \int_0 \mathrm{d}T' \frac{T'}{T}\ \mathrm{Im}\frac{-1}{\varepsilon(0,T')}\delta\left(T - T' - \hbar^2\frac{q^2}{2m}\right). \tag{24}$$

The optical energy-loss function $\mathrm{Im}[-1/\varepsilon(0,T')]$ falls off rapidly for $T' \gg T_p$ with T_p, the plasmon energy. Then the δ-function determines the Bethe ridge behavior due to electron-electron scattering at large q. There the $1/T$ factor in Eq. (23) adds another $1/q^2$ factor to the integrand of Eq. (11), which makes angular scattering fall off rapidly as $1/q^3$. At our energy of ∼8 keV, the transition from a $1/q$ to a $1/q^3$ behavior occurs at q_c, which corresponds to ∼6° scattering angle. Most of the scattering events should therefore occur within a cone of this opening angle. As long as the consecutive inelastic scattering contributions are predominantly concentrated within a cone

of 25°, the linear model should hold since cos(25°) > 0.9. Depending on the details of angular scattering this result may hold for up to ~10 inelastic scattering events. Elastic scattering is treated in Appendix C.

We note further that Eq. (24) is a valid extrapolation of the optical energy-loss function to all q since it fulfills the response function sum rule independent of q (see e.g. [29]):

$$\int_0 T\mathrm{d}T\,\mathrm{Im}\frac{-1}{\varepsilon(q,T)} = \int_0 T\mathrm{d}T \int_0 \mathrm{d}T'\frac{T'}{T}\;\mathrm{Im}\frac{-1}{\varepsilon(0,T')}\delta\left(T-T'-\hbar^2\frac{q^2}{2m}\right) = \frac{\pi}{2}T_{pZ}^2, \tag{25}$$

provided that also $\mathrm{Im}[-1/\varepsilon(0,T)]$ obeys the sum rule. Here T_{pZ} is the plasma energy calculated with all Z electrons of the atom in contrast to the plasma energy T_p calculated with the four valence electrons (see the discussion on partial sum rules following Eq. (17) in Section 4.3). Introducing Eq. (24) into Eq. (11) and making use of the δ-function in the integration over q and some rearrangements we obtain

$$W(E,T) = \frac{1}{2\pi a_0 E}\int \mathrm{d}T'\;\mathrm{Im}\frac{-1}{\varepsilon(0,T')}\frac{T'}{(T-T')T} \times\theta\left(T-T'-\frac{T'}{4E}T'\right)\theta(-T+E). \tag{26}$$

The θ-function is 0 for negative arguments and 1 otherwise. It transfers the q_- lower boundary (see Eq. (12)) of the q-integral for $T' \ll E$ to T and restricts $W(E,T)$ necessarily to the region $T \le E$. As mentioned above, we use the Ashley model without exchange, which is justified because of the large E in our application. For carbon compounds, $\mathrm{Im}-1/\varepsilon(0,T')$ falls off roughly as T'^{-4} [30] in the region 30–270 eV, and thus the contribution of the 4 valence electrons is practically exhausted before the onset of the 1s transitions. As a consequence, according to Eq. (26) $W(E,T)$ falls off to higher energies as T^{-2}. In integrating over T and interchanging the integrations, we obtain Eq. (15) and in the next step also (16).

Appendix B. Surface excitations

Surface plasmons are well established excitations of electrons penetrating the solid-vacuum interface of free-electron metals [31,32]. Such excitations will also occur in other materials. The abrupt change in dielectric response will also allow periodic surface waves with exponential damping perpendicular to the surface. In our case, the characteristic resonance character found in the spectra of ideal metals will be missing. It appears to be safe to assume that surface modes will at most be excited with the same probability or rather a lower one than in ideal metals due to higher damping. A general treatment for any material, provided the dielectric functions are known, is given in Refs. [20,33]. For free-electron metals, the material independent probability P_{sur} to excite a surface plasmon at a single surface is given by Richie [31] and Stern and Ferrell [32] as

$$P_{\mathrm{sur}} = \frac{5.8}{\sqrt{E(eV)}} \tag{27}$$

For $E = 7716$ eV, we obtain $P_{\mathrm{sur}} = 0.066$. Thus ~7% of the intensity of the elastic peak is exciting surface losses. We consider this to be an upper limit for our materials.

Appendix C. Angular spread of elastic processes

Electrons undergo elastic and inelastic scatterings. In Appendix A we have found that for several inelastic scattering events ($n = 5$, up to 10) the bulk of the trajectories will not deviate by more than 25° from a straight line. Elastic scattering, however, can change the direction of the electron trajectory.

For the purpose of our analysis, the elastic scattering-cross-section for electrons σ_{el} is essentially that of atomic C and thus can be taken to be the same for both our materials. But the elastic scattering length λ_{el} is given by $\lambda_{el}^{-1} = \rho_{At} \times \sigma_{el}$ and is thus larger by a factor of 1.54 for graphite compared to diamond. For light elements σ_{el} is close to the inelastic ionization cross-section σ_{in} for all energies above ~50 eV [6]. Indeed from the NIST data base SRD 64 [34] we obtain $\lambda_{el} = 113$ Å for graphite and 73 Å for diamond, while $\lambda_{in} \sim 100$ Å (all for $E \sim 8$ keV). For heavy elements σ_{el} is even larger and thus λ_{el} is even smaller than the IMFP. However λ_{el} is not quite the relevant quantity. Especially at high energies the angular distribution of elastic scattering is prominently peaked in the forward direction and peaking is more and more pronounced with increasing electron energy. Forward scattering does not cause appreciable deviations of the straight electron path and also thus does not alter significantly the original anisotropic angular distribution of the photoelectrons.

In transport theory, the non-forward scattering is characterized by the so-called transport mean free path (TMFP) λ_{tr} (see e.g. [6]). For graphite we obtain from the NIST data base 64 [34] $\lambda_{tr} = 9000$ Å at 8 keV. The TMFP is about two orders of magnitude larger than the IMFP. In the definition of λ_{tr} the term $(1-\cos(\varphi))$, the loss in directionality, is averaged over the full range of scattering angles. The direct effect of λ_{tr} for the break-down of our one-dimensional model is not easy to quantify. The availability of differential elastic-scattering cross-sections, however, allows analysis of the scattering in detail. For graphite, ~50% of the electrons are scattered within a cone of ~3°, and 70% within a cone of ~5°. The mean free path for not being scattered beyond 20° is 2500 Å and not beyond 45° is 5600 Å. Thus only about 4% of the electrons within one inelastic scattering length of ~100 Å will undergo angular smearing beyond 20° due to elastic scattering. Because of the higher density of diamond ($\rho^D/\rho^G = 1.54$) 6% of the elastic electrons would undergo scattering beyond 20° for diamond within the 100 Å. The deviation of the electron paths from straight lines needs to be only roughly estimated here. Within the $n = 3$ scattering lengths, which are relevant in our experiments, 84% of the electrons will remain inside the cone of 20°. For heavier elements, the elastic scattering may, however, limit a one-dimensional analysis and the influence of elastic scattering needs a more detailed attention depending on the elements in the sample.

In addition, differences between diamond and graphite in angular averaging over the anisotropic photoemission cross-section $\sigma_{in} \times p(\theta,\varphi)$ (see Eq. (1)) are also negligible.

References

[1] J. Zegenhagen, C. Kunz (Eds.), Proc. of the Workshop on Hard X-Ray Photoelectron Spectroscopy, Grenoble 2003, Nuclear Instrum. Methods Phys. Res. A 547 (2005).
[2] C.J. Powell, A. Jablonski, NIST Electron Effective-Attenuation-Length Database—Version 1.0, National Institute of Standards and Technology, Gaithersburg, MD, 2001.
[3] S. Tanuma, C.J. Powell, D.R. Penn, Surf. Interface Anal. 11 (1988) 577.
[4] S. Tanuma, C.J. Powell, D.R. Penn, Surf. Interface Anal. 20 (1993) 77.
[5] C.J. Powell, A. Jablonski, J. Phys. Chem. Ref. Data 28 (1999) 19.
[6] W.S.M. Werner, Surf. Interface Anal. 31 (2001) 141.
[7] J.-C. Kuhr, H.-J. Fitting, Phys. Stat. Sol. (a) 172 (1999) 433.
[8] J.-C. Kuhr, H.-J. Fitting, J. Electron Spectrosc. Rel. Phenom. 105 (1999) 257.
[9] S. Tanuma, C.J. Powell, D.R. Penn, Surf. Interface Anal. 37 (2005) 1.
[10] H.A. Bethe, Ann. Phys. 5 (1930) 325.
[11] D.R. Penn, Phys. Rev. B 35 (1987) 482.
[12] J.C. Ashley, J. Electron Spectrosc. Rel. Phenom. 46 (1988) 199.
[13] S. Thiess, C. Kunz, B.C.C. Cowie, T.-L. Lee, M. Renier, J. Zegenhagen, Solid State Commun. 132 (2004) 589.
[14] C. Kunz, S. Thiess, B.C.C. Cowie, T.-L. Lee, J. Zegenhagen, Nuclear Instrum Methods Phys. Res. A 547 (2005) 73.
[15] E. Wörner, E. Pleuler, C. Wild, P. Koidl, Diamond Rel. Mater. 12 (2003) 744, Nr. 3–7.

[16] CasaXPS computer program Version 2.0, October 2001, Casa Software Ltd.
[17] J.-J. Chang, D.C. Langreth, Phys. Rev. 5 (1972) 3512.
[18] J.-J. Chang, D.C. Langreth, Phys. Rev. 8 (1973) 4638.
[19] L. Hedin, J.D. Lee, J. Electron Spectrosc. Rel. Phenom. 124 (2002) 289.
[20] A. Cohen Simonsen, F. Yubero, S. Tougaard, Phys. Rev. B 56 (1997) 1612.
[21] F. Yubero, S. Tougaard, Phys. Rev. 71 (2005) 045414.
[22] F. Yubero, L. Kover, W. Drube, T. Eickhoff, S. Tougaard, Surf. Sci. 592 (2005) 1.
[23] C. Biswas, A.K. Shukla, S. Banik, V.K. Ahire, S.R. Barman, Phys. Rev. B 67 (2003) 165416.
[24] S. Doniach, M. Sunjič, J. Phys. C 3 (1970) 285.
[25] J.W. Cooper, Phys. Rev. A 42 (1990) 6942.
[26] M.B. Trzhaskovskaya, V.K. Nikulin, V.I. Nefedov, V.G. Yarzhemsky, Atomic Data Nuclear Data Tables 92 (2006) 245.
[27] M.B. Trzhaskovskaya, private communication.
[28] P. Rez, Microsc. Microanal. 9 (2003) 42.
[29] P. Nozières, D. Pines, The Theory of Quantum Liquids, Perseus Books, Massachussetts, Cambridge, 1999, p. 205.
[30] H.J. Hagemann, W. Gudat, C. Kunz, Internal Report, Deutsches Elektronen-Synchrotron DESY, Hamburg SR-74/7 (1974) and J. Opt. Soc. Am. 65 (1975) 742.
[31] R.H. Ritchie, Phys. Rev. 106 (1957) 874.
[32] E.A. Stern, R.A. Ferrell, Phys. Rev. 120 (1960) 130.
[33] Z.-J. Ding, Phys. Rev. B 55 (1997) 9999.
[34] A. Jablonski, F. Salvat, C.J. Powell, NIST Electron Elastic-Scattering Cross-Section Database—Version 3. 0, National Institute of Standards and Technology, Gaithersburg, MD, 2002.